Chinese Chemical Letters 34 (2023) 107889

Contents lists available at ScienceDirect

Chinese Chemical Letters

journal homepage: www.elsevier.com/locate/cclet

All-in-one phototheranostics based on BTP-4F-DMO nanoparticles for NIR-II fluorescence/photoacoustic dual-mode imaging and combinational therapy

Ke Yang[a,1], Bowen Yu[b,1], Wei Liu[a,1], Zequn Zhang[b], Li Huang[a], Shaojing Zhao[a], Benhua Wang[a], Jianing Yi[c,*], Jun Yuan[a,*], Yingping Zou[a], Changwei Lin[b,*], Xiangzhi Song[a], Minhuan Lan[a,*]

[a] Key Laboratory of Hunan Province for Water Environment and Agriculture Product Safety, College of Chemistry and Chemical Engineering, Central South University, Changsha 410083, China
[b] Department of Gastrointestinal Surgery, The Third Xiangya Hospital of Central South University, Changsha 410013, China
[c] Surgical Department of Breast and Thyroid Gland, Hunan Provincial People's Hospital, The First Affiliated Hospital of Hunan Normal University, Changsha 410083, China

ARTICLE INFO

Article history:
Received 4 May 2022
Revised 5 October 2022
Accepted 5 October 2022
Available online 10 October 2022

Keywords:
Photodynamic therapy
NIR-II fluorescence imaging
Photothermal therapy
Photoacoustic imaging
Autophagy-induced death

ABSTRACT

Various phototheranostics have recently been developed for phototherapy. Through proper molecular design, the photochemical and photophysical properties of these phototheranostics can be promoted. Herein, an acceptor-donor-acceptor (A-D-A)-structured dye, BTP-4F-DMO, was synthesized and prepared into water-soluble nanoparticles (NPs). The obtained BTP-4F-DMO NPs had strong absorption from 650 nm to 850 nm and a fluorescence emission peak at ~900 nm that tailed to ~1100 nm. The NPs showed a superhigh photothermal conversion efficiency of 90.5% ± 5% and could simultaneously generate $^{\bullet}OH$ and $^{1}O_2$ with a $^{1}O_2$ generation quantum yield of 4.6% under 808 nm laser irradiation. Due to these advanced properties, BTP-4F-DMO NPs can switch the role of autophagy from pro-survival to pro-death, thereby further promoting cancer cell death. These features make BTP-4F-DMO NPs a promising multifunctional phototheranostic agent for NIR-II fluorescence/photoacoustic dual-mode imaging-guided synergetic photodynamic/photothermal therapy. In general, this work provides a strategy for expanding the biomedical applications of organic A-D-A-structured phototheranostics.

Phototheranostics, which integrates optical imaging and phototherapy under light irradiation, has attracted great attention as a cancer treatment method due to its high selectivity and efficiency, noninvasiveness, negligible drug resistance, and *in situ* and real-time monitoring [1–4]. Phototherapy can be classified into photodynamic therapy (PDT) and photothermal therapy (PTT), both of which show low trauma, little tumor recurrence, and considerable therapeutic effects [5–7]. PDT utilizes photosensitizers to convert light energy to cytotoxic reactive-oxygen species (ROS) including singlet oxygen ($^{1}O_2$) and hydroxyl radicals ($^{\bullet}OH$) to kill cancer cells locally [8–11]. However, the hypoxic tumor microenvironment greatly hinders the therapeutic effect of oxygen-dependent PDT techniques in clinical medicine [12–15]. On the contrary, PTT uses light to activate photothermal agents (PTAs) to generate heat to induce tumor ablation, which shows more extensive application prospects due to its oxygen-independent property [16–18]. Moreover, the generated heat in PTT can expand blood vessels and increase the oxygen content, thus alleviating the hypoxia of tumors. The rapid heating can induce an immune response that increases the cell tolerance to heat, while the generated ROS in PDT can kill heat-resistant tumor cells (caused by heat shock proteins) to assist the therapeutic effect of PTT [19–22]. Therefore, a complementary treatment that combines PTT and PDT is expected to overcome the limitations of the individual phototherapy techniques to achieve a greater therapeutic effect [23,24].

In the other hands, growing evidence suggests that autophagy, a catabolic process that degrades dysfunctional or harmful organelles and proteins through the lysosomal pathway [25,26], plays a key role in the transition of the cell death/survival balance [27,28]. The activation of autophagy can be regarded as an important strategic

* Corresponding authors.
E-mail addresses: yijianing@hunnu.edu.cn (J. Yi), junyuan@csu.edu.cn (J. Yuan), linchangwei1987@csu.edu.cn (C. Lin), minhuanlan@csu.edu.cn (M. Lan).
[1] The authors contributed equally to this work

https://doi.org/10.1016/j.cclet.2022.107889
1001-8417/

target for cancer therapy, and thus, PDT/PTT- induced autophagy can be used to enhance the efficacy of the phototherapy [29].

All-in-one phototheranostics triggered by one laser have received great attention due to their conventional treatment, enhanced diagnostic accuracy, facile controllability, and improved treatment efficiency. Among existing diagnostic techniques, fluorescence imaging (FLI) in the second near-infrared optical window (NIR-II, 1000–1700 nm) has received more attention than the conventional FLI in the first near-infrared window (NIR-I, 650–900 nm) because of its deeper penetration and lower background signal [30,31]. Although NIR-II FLI has made great progress for the diagnosis and evaluation of tumors, it still cannot provide enough spatial resolution and sufficient scales [32]. In contrast, photoacoustic imaging (PAI) is a hybrid imaging technology that integrates optical imaging and ultrasonic imaging, which can provide much deeper tissue penetration with micro-spatial resolution [33–35]. Considering the characteristics of the two imaging technologies, the combination of NIR-II FLI and PAI can provide more accurate and richer tumor tissue information than individual techniques, and further improve the sensitivity and accuracy of cancer diagnosis [36].

Herein, we synthesized an organic molecule and prepared it into biocompatible nanoparticles (BTP-4F-DMO NPs) by modifing with polyethylene glycol (PEG) with an encapsulation yield of 68.7% [37]. As illustrated in Scheme 1a, the bandgap of BTP-4F-DMO was calculated to be 2.02 eV, making it an excellent PTA with a high photothermal conversion efficiency (PCE) of up to 90.5% ± 5%, which is much higher than many reported works (Table S1 in Supporting information). The high PCE also endowed it with excellent PAI capability. In addition, the separated HOMO and LUMO can significantly reduce the energy gap between the singlet and the triplet state (ΔE_{ST}), which is favorable for the generation of $^1O_2$ to afford effective PDT and also redshifted the absorption to the NIR region to perform PTT. The excited state energy of S_1, T_1, T_2 were caculated to be 2.1126 eV, 1.4165 eV and 1.6414 eV, respectively, through the DFT calculation of M06–2x/6–311G(d). The small $\Delta E_{S1\text{-}T1}$ of 0.69 eV and $\Delta E_{S1\text{-}T2}$ of 0.47 eV enableing the excitons easy to jump from S_1 to T_1 and T_2 through ISC process, which facilitate the production of $^1O_2$. As expected, the BTP-4F-DMO NPs can not only realize PDT with a $^1O_2$ quantum yield of 4.6% but also can generate $^{\bullet}OH$ to perform oxygen-independent PDT, which is rarely observed in the recently reported phototheranostics. After all, the reported all-in-one BTP-4F-DMO NPs realized a proper energy distribution through molecular design and thus conducted NIR-II FL/PA dual-mode imaging-guided combinational therapy of PDT and PTT (Scheme 1b).

The synthesis and characteristics of BTP-4F-DMO were presented in Figs. S1-S3 (Supporting information). The scanning electron microscope (SEM) image in Fig. 1a suggests that BTP-4F-DMO NPs have a monodisperse spherical morphology with an average diameter of ~33 nm. The absorption spectrum of the NPs in Fig. 1b revealed that BTP-4F-DMO NPs have a strong absorbance band in the NIR region from 650 nm to 850 nm and a high molar absorption coefficient of 2.17×10^5 L mol^{-1} cm^{-1}. Besides, BTP-4F-DMO NPs can emit strong fluorescence with a peak at ~900 nm tailed to ~1100 nm (Fig. 1c), which make BTP-4F-DMO NPs suitable for NIR-II FLI.

The strong absorbance at the NIR region makes BTP-4F-DMO NPs a superior PTA. As shown in Fig. 1d and Fig. S4 (Supporting information), the temperature of 8 μmol/L BTP-4F-DMO NPs solution increased to about 90 °C after irradiation for 10 min, while the temperature of pure water increased by only 2 °C. Moreover, the BTP-4F-DMO NPs aqueous solution also exhibited excellent photostability. As shown in Fig. 1e, BTP-4F-DMO NPs reached the same peak temperature even after six cycles of irradiation, while the temperature of the Indocyanine Green (ICG) weakened after only one illumination cycle. Furthermore, the absorption spectra of BTP-4F-DMO NPs showed no obvious changes after six cycles, while the absorbance of ICG decreased by more than 95% (Fig. S5 in Supporting information), indicating that BTP-4F-DMO NPs were very stable compared with ICG (Fig. 1f). Furthermore, the absorption spectra and particle sizes showed no obvious changes within 6 days stored at room temperature (Fig. S6 in Supporting information).

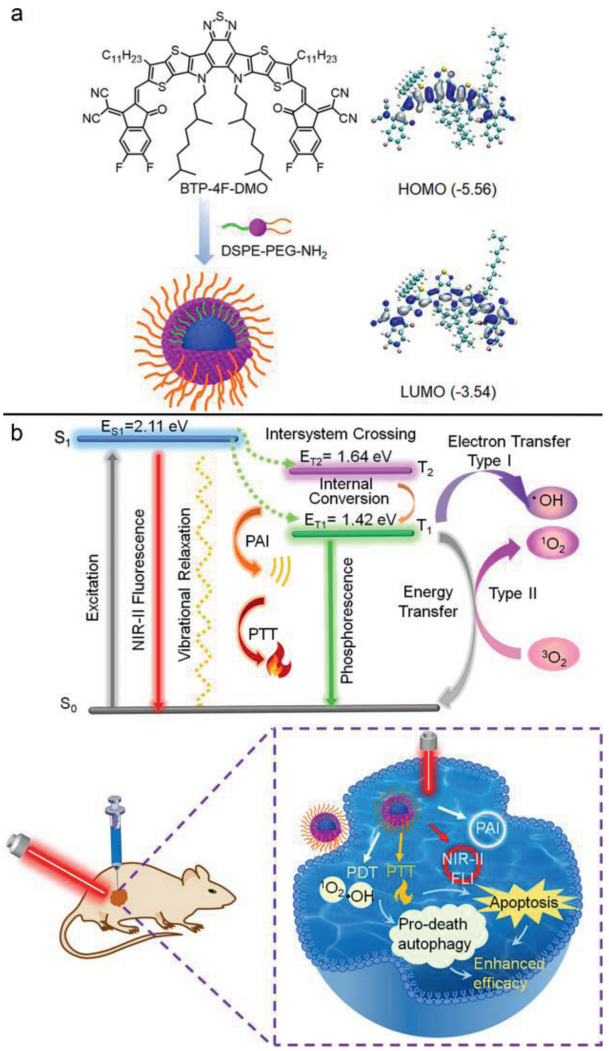

Scheme 1. (a) Molecular structure of BTP-4F-DMO and the preparation of BTP-4F-DMO NPs (left), and frontier molecular orbital electron density distribution of BTP-4F-DMO molecule (right). (b) Mechanism of BTP-4F-DMO NPs-based NIR-II FLI, PAI, PDT, PTT, and its applications.

To assess the photothermal performance of BTP-4F-DMO NPs, the PCE was calculated. In detailed, the BTP-4F-DMO NPs solution was continuously irradiated for 10 min with temperature monitored, and the PCE of BTP-4F-DMO NPs was calculated to be 90.5% ± 5% (Fig. S7a in Supporting information). These results demonstrated the excellent PCE and good photostability of the BTP-4F-DMO NPs, making it a potential candidate for PTT application. Then, FITC-labeled phalloidin was used to evaluate the photothermal effect of NPs on cells. As expected, the excellent photothermal conversion capability of the NPs introduces good photothermal therapeutic. As shown in Fig. 1g, the cells of PBS, PBS + Laser, and NPs groups showed a rigid cytoskeleton, while only the NPs + Laser group showed skeleton collapse, indicating the effect of heat-induced breakage [38].

The ROS generation capability is an important criterion for evaluating the PDT effect. SOSG was employed to evaluate the $^1O_2$

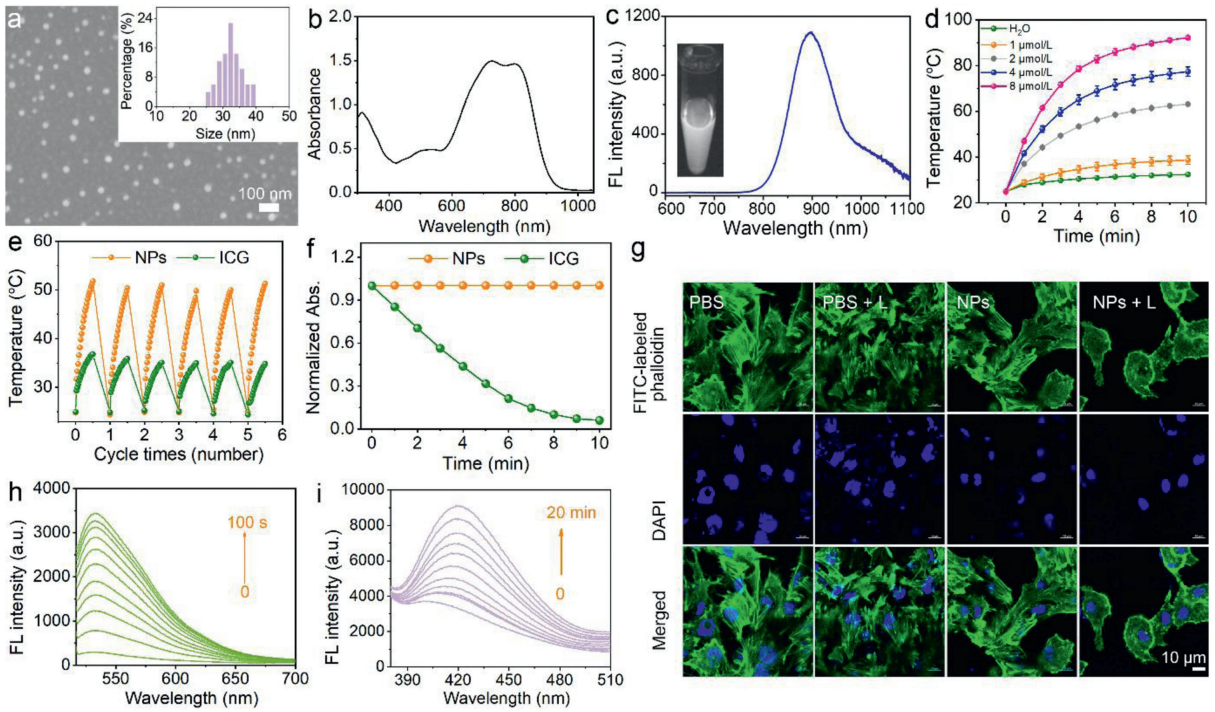

Fig. 1. (a) SEM image and size distribution histogram of the BTP-4F-DMO NPs. (b) The absorption and (c) fluorescence spectra of BTP-4F-DMO NPs (λ_{ex}: 532 nm). The inset picture in (c) is a fluorescence image of BTP-4F-DMO NPs solution in a centrifuge tube (λ_{ex}: 808 nm). (d) Photothermal effect of BTP-4F-DMO NPs at different concentrations (808 nm, 1.0 W/cm^2). (e) Temperature variations in the solution of BTP-4F-DMO NPs and ICG irradiated for 6 cycles (808 nm, 0.5 W/cm^2). (f) The normalized absorbance change of BTP-4F-DMO NPs and ICG upon prolonging the irradiation time. (g) FITC-labeled phalloidin and DAPI co-stained with 4T1 cells after various treatments as indicated. Changes of the fluorescence intensity of BTP-4F-DMO NPs + (h) SOSG (λ_{ex}: 504 nm) and (i) TA (λ_{ex}: 330 nm) under 808 nm laser irradiation.

generation performance of BTP-4F-DMO NPs. As presented in Fig. 1h, the fluorescence intensity of the SOSG containing BTP-4F-DMO NPs solution increased during continuous 808 nm laser irradiation. After only 100 s irradiation, the fluorescence intensity increased by 12 times, indicating that BTP-4F-DMO NPs had a strong $^1O_2$ production ability. In contrast, the fluorescence intensity of SOSG alone or SOSG containing ICG solutions showed a negligible increase (Fig. S7b in Supporting information). As further confirmed in Fig. S7c (Supporting information), the characteristic peak at 1270 nm demonstrated that BTP-4F-DMO NPs can effectively generate $^1O_2$, with a quantum yield of 4.6%.

To verify the ability of the NPs to generate $^{\bullet}$OH, terephthalic acid (TA), a typical $^{\bullet}$OH scavenger, was used to trap $^{\bullet}$OH by forming hydroxycyctohexadienyl. As shown in Fig. 1i, the fluorescence intensity of TA-containing BTP-4F-DMO NPs increased gradually upon extending the irradiation time, while that of TA alone (control) remained nearly unchanged (Fig. S7d in Supporting information), indicating that BTP-4F-DMO NPs can produce $^{\bullet}$OH under 808 nm laser irradiation. Moreover, the ROS generation ability of the BTP-4F-DMO NPs in living cells was further confirmed by using DCFH-DA as an indicator. As shown in Fig. S8 (Supporting information), there was a bright green fluorescence in groups treated with BTP-4F-DMO NPs + laser irradiation, which confirmed ROS generation in the cells, while there was almost no green fluorescence in the control groups. Furthermore, the intracellular $^1O_2$ and $^{\bullet}$OH generation abilities were separately detected by using O22 and O28 as the indicators. As shown in Fig. S9 (Supporting information), obvious fluorescence only appeared in the NPs + Laser group, which can elucidate that BTP-4F-DMO NPs have the intracellular ROS generation ability, and thus can be applied for both Type I/II PDT.

The cytotoxicity of BTP-4F-DMO NPs against 4T1 cells under 1 W/cm^2 light irradiation was investigated. As shown in Fig. 2a, the cell viability remained over 90% after incubation with BTP-4F-DMO NPs (10 μmol/L) without laser irradiation, while decreased to 8% when exposed to 808 nm laser irradiation for 10 min. BTP-4F-DMO NPs *in situ* photo-generates ROS and subsequently trigger cancer cell apoptosis were detected by utilizing Calcein-AM (live cells, green) and PI (dead cells, red) staining. As shown in Fig. 2b(I), the control group contained mostly living cells, while there were many dead cells in the BTP-4F-DMO NPs + light group, which was consonant with previous results. Then, the effect of BTP-4F-DMO NPs on proliferation was determined by 5-ethynyl-2′-deoxyuridine (EdU) staining. As shown in Fig. 2b(II), the cells incubated with BTP-4F-DMO NPs showed green fluorescence after laser irradiation, indicating the inhibition of cell proliferation. Furthermore, the cell death mechanism was investigated *via* quantitative flow cytometry by using the V-FITC/7-AAD assay. As demonstrated in Fig. 2c, the other control group maintained a high cell viability, while the apoptosis/necrosis rate of cells treated with NPs and laser irradiation was as high as 80.53%.

To further comprehend the mechanism of the therapeutic effect of BTP-4F-DMO NPs, the autophagy levels of 4T1 cells with different treatments were then investigated. Autophagy-related proteins, LC3 and p62, were determined by Western blot assay to investigate the conversion of LC3-I to LC3-II and the degradation of the autophagy substrate p62 during the autophagy process. As shown in Fig. 2d, BTP-4F-DMO NPs with irradiation could induce cellular autophagy, which was confirmed by the increase of the LC3-II/β-actin and the down-regulation of p62 expression (Fig. S10 in Supporting information). Afterward, we transfected the RFP-GFP-LC3 plasmid to further confirm changes in the intracellular autophagic flux. By using this plasmid to label autophagic vacuoles in cells, normal punctate autophagic vacuoles appeared yellow (RFP and GFP superimposed). When the autophagosome fuses with the lysosome, the pH-sensitive GFP will be quenched and will not emit light, while

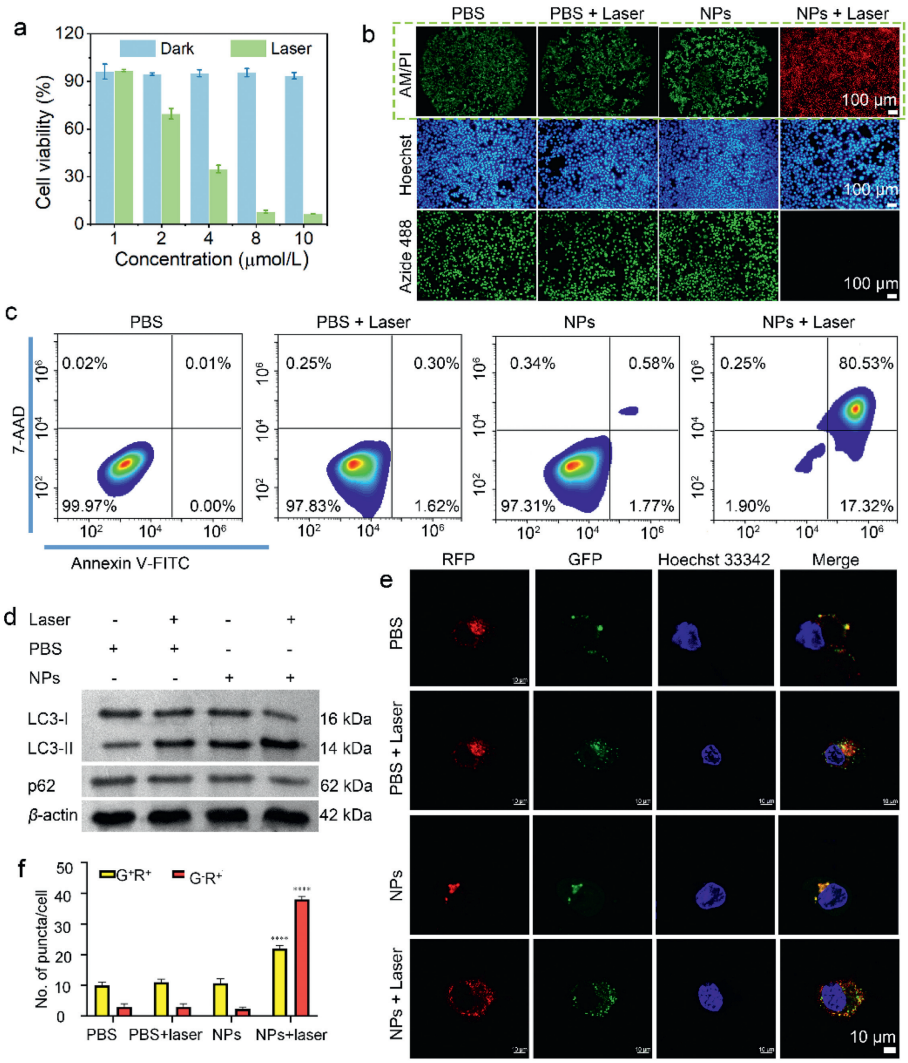

Fig. 2. (a) Cytotoxicity assays of BTP-4F-DMO NPs against 4T1 tumor cells with or without laser irradiation. (b) Fluorescence images of (i) Calcein-AM and PI and (ii) EdU staining with 4T1 cells. (c) Apoptotic rates of 4T1 cells under different conditions (808 nm, 1.0 W/cm^2, 10 min). (d) The expression of LC3-II/I and p62 was evaluated by Western blot analysis after different treatments. (e) Fluorescence images and (f) intensities of 4T1 cells after incubation with BTP-4F-DMO NPs with/without laser irradiation. Scale bar = 10 μm. $^{****}P < 0.0001$. Error bars correspond to standard deviations with $n = 3$.

the RFP-GFP-LC3 will appear red to form autophagolysosomes. As shown in Figs. 2e and f, the increased immunofluorescence of the intracellular autophagic vacuoles (yellow) and autophagylysosomes (red) showed that the BTP-4F-DMO NPs + Laser group enhanced autophagy after RFP-GFP-LC3 plasmid transfection with the comparison with the other three groups.

Due to the lack of tumor targeting probe, the BTP-4F-DMO NPs exhibit no obvious tumor targetability. As shown in Fig. S11 (Supporting information), BTP-4F-DMO NPs mainly distributed in liver and spleen after intravenous injection. However, there is no obvious aggregation in tumor region. Based on that, the *in vivo* imaging and phototherapeutic efficacy of BTP-4F-DMO NPs were investigated by using intratumoral injection, and all the animal experiments were approved by the Ethics Committee for Experimental Animal Welfare of Central South University. In addition, the intratumoral injection could improve the enrichment of drugs in the tumor site and avoid accumulating in other tissue.

As shown in Fig. 3a, the tumor region was visible from the surrounding background tissue within 10 min, suggesting that the BTP-4F-DMO NPs could be used to construct NIR-II fluroescent probes for *in vivo* imaging. Subsequently, PAI was performed in living mice. As expected, after intra-tumoral injection of BTP-4F-DMO NPs, a strong PA signal at the tumor site was observed (Fig. 3b), showing that BTP-4F-DMO NPs can potentially be used in PAI diagnosis. Subsequently, we further investigated the *in vivo* photothermal imaging ability of BTP-4F-DMO NPs. The tumor-bearing mice injected with BTP-4F-DMO NPs (10 μmol/L) were irradiated by the 808 nm laser (1 W/cm^2) for 10 min. As shown in Fig. 3c, the tumor temperature distinctly increased to ~60 °C, which is high enough to ablate the tumor thoroughly.

The phototherapeutic efficacy of BTP-4F-DMO NPs in living mice was further studied. The Balb/C mice were randomly divided into groups of saline, saline + laser, BTP-4F-DMO NPs (10 μmol/L), and BTP-4F-DMO NPs + laser. As shown in Fig. 3d, the tumor volumes in the BTP-4F-DMO NPs + laser group decreased to nearly 0, whereas the other groups showed an increasing trend. The tumor peeling off after 13 days could also further confirm the above results (Fig. S12 in Supporting information). To further verify the therapeutic effect of BTP-4F-DMO NPs, the tumors were peeled off from differently treated mice to conduct H&E and Ki67 analyses. As shown in Fig. 3e, the tumor slices of H&E results of the NPs + Laser group showed a distinct necrotic region, and the Ki67 analysis exhibited obvious proliferation inhibition, whereas the other groups showed no differences compared with the control group. These re-

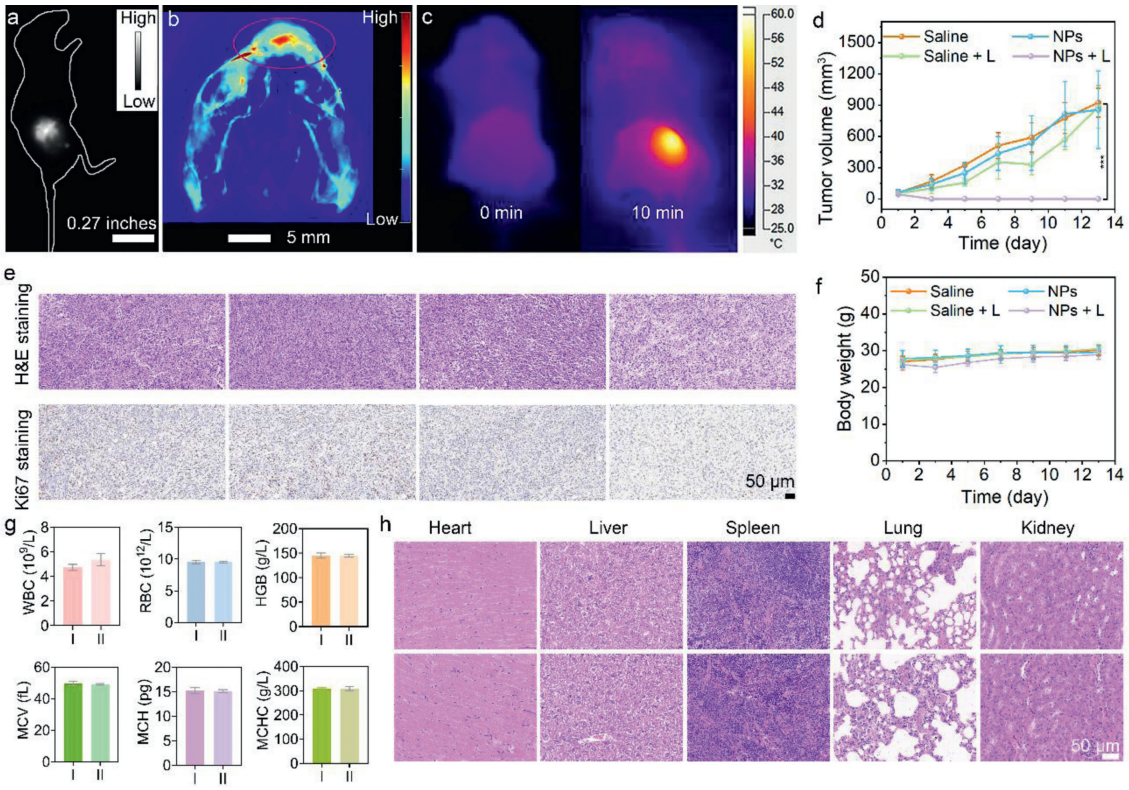

Fig. 3. (a) NIR-II FLI and (b) PAI of BTP-4F-DMO NPs in 4T1 tumor mice. (c) The thermal images of mice injected with BTP-4F-DMO NPs irradiated for 0 min (left) and 10 min (right). Time-dependent (d) tumor volume and (f) bodyweight changes of the mice. (e) H&E and Ki67 analyses results. (g) Blood routine analysis results. (h) The H&E staining of major organs. up: control; down: BTP-4F-DMO NPs.

sults demonstrated that the BTP-4F-DMO NPs can effectively kill the tumors and inhibit cell growth.

The biosafety of BTP-4F-DMO NPs was further assessed. As shown in Fig. 3f, the body weights of mice from different treatment groups showed inconspicuous changes throughout the whole therapy, indicating the sufficient biosafety of BTP-4F-DMO NPs in living systems. In addition, the results of blood routine analysis (Fig. 3g) and organ slicing (Fig. 3h) showed that BTP-4F-DMO NPs held negligible harm to mice. The above results collectively indicate that BTP-4F-DMO NPs can be safely used in therapies without producing evident systemic toxicity.

Here, a novel organic dye, BTP-4F-DMO, was successfully synthesized. To improve its biocompatibility, we functionalized it with polyethylene glycol and obtained BTP-4F-DMO NPs. The prepared BTP-4F-DMO NPs could not only be used as a NIR-II FL and PAI agents, but also as a PDT/PTT combinational therapy agents. Under single-laser irradiation (808 nm), the BTP-4F-DMO NPs possess the generation ability of $^1O_2$ and $^{\bullet}OH$. In addition, the excellent PCE ($\eta = 90.5\% \pm 5\%$) of BTP-4F-DMO NPs give it superior phototherapeutic effects for tumor elimination in live mice. Furthermore, we proposed an innovative strategy to improve the therapeutic efficacy by inducing autophagy hyperactivation to switch autophagy from pro-survival to pro-death. The increased expression of LC3-II/β-actin and the decrease of p62 indicated that the autophagy level was significantly increased after the combined treatment of PTT and PDT. In general, the integrated phototherapy triggered by a single 808 nm laser developed in this work shows advantages for cancer treatment.

Declaration of competing interest

The authors declare that they have no known competing financial interests or personal relationships that could have appeared to influence the work reported in this paper.

Acknowledgments

This work was supported by the National Natural Science Foundation of China (Nos. 61805287 and 62175262), the Innovation-Driven Project of Central South University (No. 2020CX021).

Supplementary materials

Supplementary material associated with this article can be found, in the online version, at doi:10.1016/j.cclet.2022.107889.

References

[1] M.H. Lan, S.J. Zhao, W.M. Liu, et al., Adv. Healthc. Mater. 8 (2019) 1900132.
[2] S.B. Brown, E.A. Brown, I. Walker, Lancet Oncol. 5 (2004) 497–508.
[3] J. Li, K. Pu, Chem. Soc. Rev. 48 (2019) 38–71.
[4] Y. Zhang, X. Zhang, H. Yang, et al., Chem. Soc. Rev. 50 (2021) 11227–11248.
[5] B.L. Li, S.J. Zhao, L. Huang, et al., Chem. Eng. J. 408 (2020) 127245.
[6] S.L. Higgins, K.J. Brewer, Angew. Chem. Int. Ed. 51 (2012) 11420–11422.
[7] X. Li, J.F. Lovell, J. Yoon, X.Y. Chen, Nat. Rev. Clin. Oncol. 17 (2020) 657–674.
[8] Y.M. Wen, Q.Y. Jia, F.C. Nan, et al., Chem. Asian J. 14 (2019) 2162–2168.
[9] J. Ge, Q. Jia, W. Liu, et al., Adv. Mater. 27 (2015) 4169–4177.
[10] J.M. Chen, T.J. Fan, Z.J. Xie, et al., Biomaterials 237 (2020) 119827.
[11] Y. Xu, W. Tuo, L. Yang, et al., Angew. Chem. Int. Ed. 61 (2022) e202110048.
[12] L. Huang, S. Zhao, J. Wu, et al., Coord. Chem. Rev. 438 (2021) 213888.
[13] Y. Zhang, F. Wang, C. Liu, et al., ACS Nano 12 (2018) 651–661.
[14] X. Li, N. Kwon, T. Guo, Z. Liu, J.Y. Yoon, Angew. Chem. Int. Ed. 57 (2018) 11522–11531.
[15] C. Li, Y. Xu, L. Tu, et al., Chem. Sci. 13 (2022) 6541–6549.
[16] H.S. Jung, P. Verwilst, A. Sharma, et al., Chem. Soc. Rev. 47 (2018) 2280–2297.
[17] J. Li, C. Xie, J. Huang, et al., Angew. Chem. Int. Ed. 57 (2018) 3995–3998.
[18] S. Liu, X. Pan, H. Liu, Angew. Chem. Int. Ed. 59 (2020) 5890–5900.
[19] H. He, S. Ji, Y. He, et al., Adv. Mater. 29 (2017) 1606690.
[20] W.S. Chen, J. Ouyang, H. Liu, et al., Adv. Mater. 29 (2017) 1603864.
[21] M. Zhao, Y. Xu, M. Xie, et al., Adv. Healthc. Mater. 7 (2018) 1800606.
[22] K. Yang, S. Zhao, B. Li, et al., Coord. Chem. Rev. 454 (2022) 214330.
[23] M.R. Younis, C. Wang, R. An, et al., ACS Nano 13 (2019) 2544–2557.
[24] Z. Xie, T. Fan, J. An, et al., Chem. Soc. Rev. 49 (2020) 8065–8087.
[25] T. Yu, F. Guo, Y. Yu, et al., Cell 170 (2017) 548–563.
[26] M.T. Rosenfeldt, J. O'Prey, J.P. Morton, et al., Nature 504 (2013) 296–300.
[27] Y. Duo, M. Yang, Z. Du, et al., Acta Biomater. 79 (2018) 317–330.

[28] Y. Wang, Y.X. Lin, J. Wang, et al., ACS Nano 13 (2019) 7568–7577.
[29] Y. Wang, Y.X. Lin, Z.Y. Qiao, et al., Adv. Mater. 27 (2015) 2627–2634.
[30] Q. Wang, Y. Dai, J. Xu, et al., Adv. Funct. Mater. 29 (2019) 1901480.
[31] Y. Tang, Y. Li, X. Hu, et al., Adv. Mater. 30 (2018) 1801140.
[32] S. He, J. Song, J. Qu, Z. Cheng, Chem. Soc. Rev. 47 (2018) 4258–4278.
[33] Z. Sheng, B. Guo, D. Hu, et al., Adv. Mater. 30 (2018) 1800766.
[34] Z. Yang, Y. Dai, C. Yin, et al., Adv. Mater. 30 (2018) 1707509.
[35] C. Yin, X. Zhen, Q. Fan, W. Huang, K.Y. Pu, ACS Nano 11 (2017) 4174–4182.
[36] X. Ge, Q. Fu, L. Su, et al., Theranostics 10 (2020) 4809–4821.
[37] D.M. Zhu, W. Xie, Y.S. Xiao, et al., Nanotechnology 29 (2018) 084002.
[38] Y.W. Bao, X.W. Hua, X. Chen, F.G. Wu, Biomaterials 183 (2018) 30–42.